Theoretical and Applied Fracture Mechanics 118 (2022) 103273

Contents lists available at ScienceDirect

Theoretical and Applied Fracture Mechanics

journal homepage: www.elsevier.com/locate/tafmec

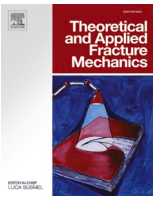

Critical plane based method for multiaxial fatigue analysis of 316 stainless steel

A.S. Cruces [a], A. Garcia-Gonzalez [a], B. Moreno [a], T. Itoh [b], P. Lopez-Crespo [a,*]

[a] Department of Civil and Materials Engineering, University of Malaga, C/Dr Ortiz Ramos s/n, 29071 Malaga, Spain
[b] Department of Mechanical Engineering, College of Science and Engineering, Ritsumeikan University, Kusatsu-shi, Shiga, Japan

ARTICLE INFO

Keywords:
Biaxial fatigue
316 stainless steel
Critical plane methods
Mean stress

ABSTRACT

In this work, the fatigue behaviour of 316 stainless steel is studied with different critical plane models. Seven cylindrical samples were used for the study, being subjected to different complex loading paths, generating combined stresses along the axial and transversal sample directions, these being: individual axial stress, individual hoop stress, alternating axial and hoop stress, a proportional combination of axial and hoop stress, and a non-proportional combination of L-shaped and square-shaped axial and hoop stress. The fatigue analysis is performed using five critical plane models; named Fatemi-Socie, Varvani-Farahani, Gan-Wu-Zhong, Liu I and Liu II. The models were assessed based on their fatigue life and crack angle prediction capacity. The Gan-Wu-Zhong recently proposed critical plane model was examined and provided acceptable results for the multiaxial loads tested on 316 steel. Nevertheless, Fatemi-Socie produced the most accurate results in terms of cracking orientation and Liu II gave the best fatigue life predictions.

1. Introduction

Uniaxial cyclic tests are the first step in characterising different metals' fatigue behaviour. Fatigue properties obtained from these tests are usually adequate, as service loads are frequently relatively simple [1]. In other cases, existing uncertainties are compensated by safety coefficients. However, more precise material data must be obtained when there are greater in-service demands on the component [2,3]. Fatigue life can vary significantly for the same level of material deformation or stress, depending on the mode of application of loads during the cycle [4,5]. Additionally, the change of principal stress direction along a cycle can produce additional hardening in the material [6]. Thus, the further the in-service loading conditions are from those of the test where the fatigue values used were obtained, the greater the margin for error – depending on the material. Ideally, models which allow the characterisation of material fatigue behaviour under complex loading conditions should be obtained from simple experimental data, such as uniaxial data. Critical plane methods have been successfully applied in this sense for different types of materials and service conditions. M. Firat applies these models for the fatigue design of wheels made of different materials [7,8]. Carpinteri and Spagnoli proposed and applied a critical plane model, returning a good agreement between experimental and calculated fatigue life to welded joints subjected to multiaxial fatigue [9]. These models are also included in R. Branco's recent studies, with 18Ni300 produced using selective laser melting [10]. These methods are based on the observation of mechanisms involved in the nucleation and growth of cracks, thus capable of predicting not only the material's fatigue life, but also the initial angle of crack growth. Depending on the type of material, some materials will show a greater dominance of certain mechanisms throughout the fatigue process, so models that respond better to certain types of materials must be chosen [11].

316 stainless steel is used in industry for structural and piping applications due to its excellent corrosion resistance and mechanical properties. Morishita studied the fatigue life of 316 stainless steel with various proportional and non-proportional loading paths under inner and outer pressure [12]. This material also exhibits a good response at high temperature. Creep models for 316L were developed, and extended to creep-fatigue to estimate fatigue life [13]. The multiaxial behaviour of 316L stainless steel was also investigated, with different critical plane models under strain control [14].

In this work, a study is carried out on the fatigue life and initial crack growth angle prediction. The analysis is performed on 316 stainless steel. Part of the novelty of this work is owed to the complexity of load combination that is applied to the different specimens. Some of the load

* Corresponding author.
E-mail address: plopezcrespo@uma.es (P. Lopez-Crespo).

https://doi.org/10.1016/j.tafmec.2022.103273
Received 23 October 2021; Received in revised form 15 January 2022; Accepted 26 January 2022
Available online 31 January 2022

combinations presented are rarely tested in research works and are very helpful to understand the behaviour of 316 steel under real complex loading conditions. Quantifying the proportional and non proportional stress and strain contributions requires the use of critical plane methods. To this end five different critical plane models are tested [15–18], four of them being energy-based. The results allow the efficacy of the different models to be compared, both in terms of life prediction and in terms of crack orientation. This latter subject, the orientation of the crack, is one of the main features of critical plane models but most works do not make use of it. Nevertheless, the crack orientation is essential to fully characterise the fatigue behaviour of materials, to the point that a series of international conferences are fully devoted to crack paths [19,20].

Experimental 316 stainless steel data have been used for the study. Tests are uniaxial and multiaxial, with proportional and non-proportional loads. The initial crack growth angles were measured by optical microscopy and compared with the values predicted by the different models.

2. Materials and methods

The material used in the research was 316 stainless steel with a quenching heat treatment. This is a widely used material in different sectors, including aerospace, nuclear, power stations and offshore structures. The chemical composition is shown in Table 1. The monotonic properties of the material are shown in Table 2 and were obtained from experimental testing.

Multiaxial fatigue tests were conducted under stress control with tubular specimens based on ASTM axial–torsional fatigue tests [21]. Surface roughness has an average value of 1.6 μm on the gauge area. The testing machine (Fig. 1), with three actuators, allows the use of: (i) axial force, (ii) reversed torsion and (iii) inner pressure on the sample. The sample directions considered in the work are the Z-direction along the sample axis, R-direction for the radial direction of the section and θ-direction perpendicular to the Z- and R-directions. These three directions generate the coordinate system considered to calculate local stresses and strains. The tests used in this work only include cases of axial force and inner pressure. Inner pressure produces a radial force along the thickness in the R direction, with the maximum value on the inner surface and zero on the outer surface. Simultaneously, a hoop stress in the θ-direction, with a higher value in the inner surface, is generated. Axial force produces a distributed normal stress in the Z-direction, perpendicular to the θR plane. Fig. 1 also shows the dimensions of the specimen. The hoop stress is assumed to be uniform given the thinness of the cylinder wall in the gauge length.

Monotonic and cyclic properties are shown in Table 3. Torsional cyclic properties were derived from tensile values [22].

Six different loading paths were performed under force/pressure control while measuring the axial and hoop strains on the outer surface. Fig. 2 shows a diagram of the loading paths studied in this work, pulsating uniaxial load in the Z- and θ-directions, total inversion in the Z-direction, combining axial and inner pressure with square-shape and L-shape with traction and compression axial load. Hoop and radial stresses are calculated considering thick-walled cylinders [23]. All experiments were conducted at room temperature. The loading frequency was 0.4 Hz for all tests except for loading path 4 (Fig. 2) where the frequency was 0.2 Hz. The inner pressure was applied by pumping oil inside the hollow specimens. The strain were continuosly evaluated with the help of extensometers. Table 4 shows the loading paths applied, the test identification ID, the axial stress range $\Delta\sigma_Z$, the hoop stress range $\Delta\sigma_\theta$, the range and mean strain for axial and hoop direction at half-life fatigue on the outer surface $\Delta\varepsilon_z$, ε_{zm}, $\Delta\varepsilon_\theta$ and $\varepsilon_{\theta m}$ and total fatigue life N_f for each test. The axial and hoop stresses were calculated assuming thin walled cylinder [24] as follows:

$$\sigma_Z = \frac{F}{\pi\left(r_o^2 - r_i^2\right)} + \frac{Pr_i^2}{r_o^2 - r_i^2} \quad (1)$$

$$\sigma_\theta = \frac{Pr_i^2}{r_o^2 - r_i^2}\left[1 + \frac{r_o^2}{r^2}\right] \quad (2)$$

where F is the force applied, P the inner pressure introduced, r_o the outer radius, r_i the inner radius and r is the radius where the hoop and radial stresses are calculated. Fatigue failure was detected by a 50% pressure drop in the sample. This way of detecting the failure was found to be the most consistent for the experimental setup employed. Eventhough paths 1 and 3 did not include any inner pressure, a very small inner pressure was applied so that the failure criterion was the same for all tests. Tests 1 and 3, without inner pressure along the loading path, include a minimum inner pressure value to use the same fail criteria. Loading path 1 and 2 are defined to generate the same stress range on the outer surface, but in different directions. As previously stated, the inner pressure produces a higher local stress level on the inner surface. Accordingly, the sample's final fatigue life is lower for said loading path. Although the stress range considered on the outer surface is the same, the strain range generated is different, and can be correlated with the fatigue life. As all critical plane models studied include strain ranges in the damage parameter, the error to consider the outer surface for the fatigue predictions will be reduced. Regardless, this point will be considered in the final results.

Fig. 3 shows the σ-ε curves at half-life fatigue in the in the z and θ directions for each loading path. The curves for paths 1 and 3 showed a very noisy loop. This is due to the poor signal to noise ratio of the load cell in the θ direction at such low range (note the small vertical scale in the σ_θ curve for paths 1 and 3 in Fig. 3). Similar behaviour was observed on the σ_z curve for the path 2, because the longitudinal load was very small. The load path 1 shows a hysteresis loop shifted on both directions as a consequence of the mean strain ($\varepsilon_{zm} = 0.0762$ and $\varepsilon_{\theta m} = -0.016$ in Table 4). For the loading path 2, the hysteresis loop in the θ direction is narrower than that observed for path 1, even though the strain values are larger for path 2 ($\Delta\varepsilon\theta = 0.0054$) than for path 1 ($\Delta\varepsilon z = 0.0034$) and the stress values were similar. The load path 3 shows a hysteresis loop with a significant mean strain accumulated in the z direction. Such strain is probably due to the higher level of applied stress. For the load paths where stresses are combined in alternative steps in the two directions (paths 4, 5 and 6), the curves observed in the two directions are similar. For the load path 4, the base of the rhomboid is the strain caused by the stress in the orthogonal direction. For the load path 5, the combined effect of the tensile stress in both directions generates an increment of the total strain in both directions, as noticed by the larger hysteresis loop as compared to that of the path 2. Fig. 3 also shows that the hysteresis loop is narrower for the load path 6A than for the load path 5. The path 6A also shows that no permanent strain in the θ direction was measured after the load applied in the z direction. This is in contrast to the evolution observed in path 5. For the sake of brevity, the path 6B was not included since it was very similar to 6A but with higher strain levels.

Once the specimens are tested, the crack growth angles are

Table 1
Chemical composition in 316 stainless steel (in wt%).

C	Si	Mn	P	S	Cr	Ni	Mo
0.06	0.46	1.33	0.32	0.25	16.97	10.15	2.03

Table 2
Monotonic properties of 316 stainless steel.

Property	Value
Yield strength, σ_y	240 MPa
Tensile strength, σ_{uts}	597 MPa
Young's Modulus, E	193GPa
Shear Modulus, G	75GPa
Poisson's ratio in the elastic regime, ν_e	0.3
Poisson's ratio in the plastic regime, ν_p	0.5

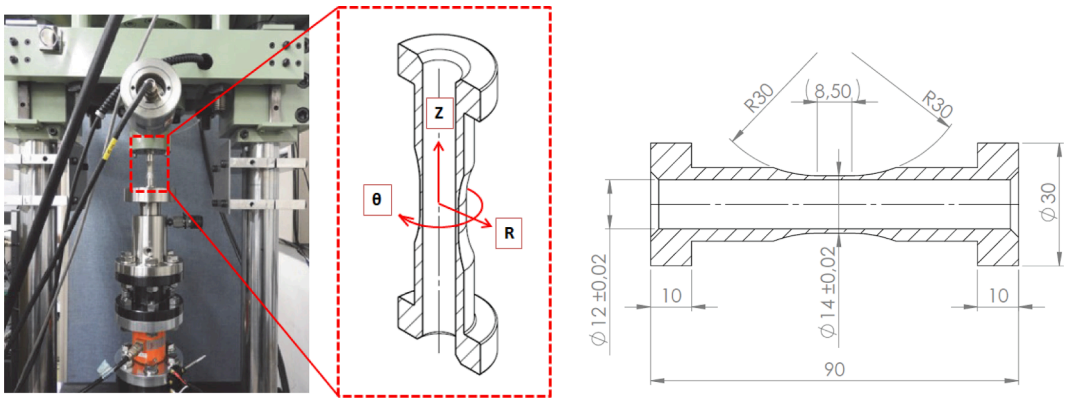

Fig. 1. Experimental setup, sample directions considered in the work and sample dimensions (in mm).

Table 3
Tensional cyclic mechanical properties of 316 stainless steel.

Property	Value
Fatigue strength coefficient, σ'_f	663.25 MPa
Fatigue strength exponent, b	−0.093
Fatigue ductility coefficient, ε'_f	0.1895
Fatigue ductility exponent, c	−0.4657

measured. The first angle is measured directly on the specimen's surface. The second angle, which determines the initial crack growth plane, requires a transverse or longitudinal cut of the specimen, depending on the test type. To do so, a cut is made in the middle of the crack observed on the surface. A Struers Accutom-2 cutting machine with a disc speed of 400 rpm was used for this purporse. Once the specimen section featuring the through crack has been cut, the surface is prepared to clearly observe the crack angle. Samples are embedded in Bakelite at 180 °C for 10 min, then polished in a Struers Tegrapol-11 polishing machine. Steps followed consisted of an initial grinding with #800 SiC sandpaper, and successive suspension of 4 μm size polishing particles. After polishing the surface, images of the surface were taken at different magnifications with a DSLR Canon EOS2000D with 24MP mounted in a Nikon Epiphot 280 with an LMScope adaptor. The initial growth angle was measured using ImageJ software [2]. Sample 4 (Fig. 4 (D)) showed large plastic deformation. As a result, the distance between the crack faces was larger than for the other samples. This made the two crack flanks too far apart to be included in the same frame at 400X, unlike the rest of images in Fig. 4. Consequently, Fig. 4 (D) only shows the top crack face. Anyway, this is enough for measuring the crack angle at initiation, because the angles measured on the top and bottom faces coincide. For tests with a loading path including inner pressure, the crack is always oriented approximately perpendicular to the θR plane.

3. Critical plane models

The analysis consists of evaluating the damage in different planes and choosing the plane where maximum damage occurs; namely the critical plane [22]. The location of the critical plane changes depending on the fatigue stage, type of material and loading conditions [25]. For ductile materials, the dominant failure plane favours maximising the shear strain or mode II/III strain. For brittle materials, the dominant failure plane favours maximising the normal strain or mode I strain. In the present work, the critical plane is considered the plane with the higher damage parameter along the cycle. These criteria affect the original model criteria to define the critical plane, except for the Gan-Wu-Zhong model [17].

3.1. Fatemi-Socie model

The Fatemi-Socie model was chosen as it has been proven to generate good predictions for different metals, and includes the mean stress effect in the damage parameter [14,26,27]. The Fatemi-Socie model is an equivalent strain type of model and is based on mode II/III failure. The critical plane is defined from the plane where the shear strain is

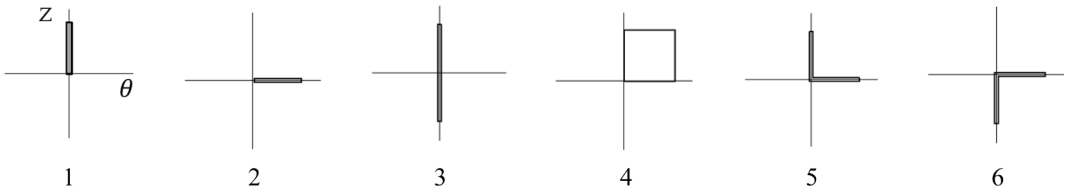

Fig. 2. Loading paths for samples.

Table 4
Test details of the loading path.

Path	$\Delta\sigma_z$	$\Delta\sigma_\theta$	$\Delta\varepsilon_z$	$\Delta\varepsilon_\theta$	ε_{zm}	$\varepsilon_{\theta m}$	N_f
1	445.15	1.83	0.0034	0.00060	0.076	−0.016	159,600
2	2.39	450.32	0.0022	0.0054	−0.0080	0.051	29,300
3	884.49	1.41	0.016	0.0039	0.11	−0.022	393
4	373.95	413.12	0.0044	0.0036	0.067	0.043	8,400
5	349.30	346.09	0.0040	0.0058	0.0040	0.034	14,486
6A	399.76	450.21	0.0020	0.0048	−0.030	0.053	25,770
6B	442.64	511.01	0.0024	0.0048	−0.057	0.062	13,542

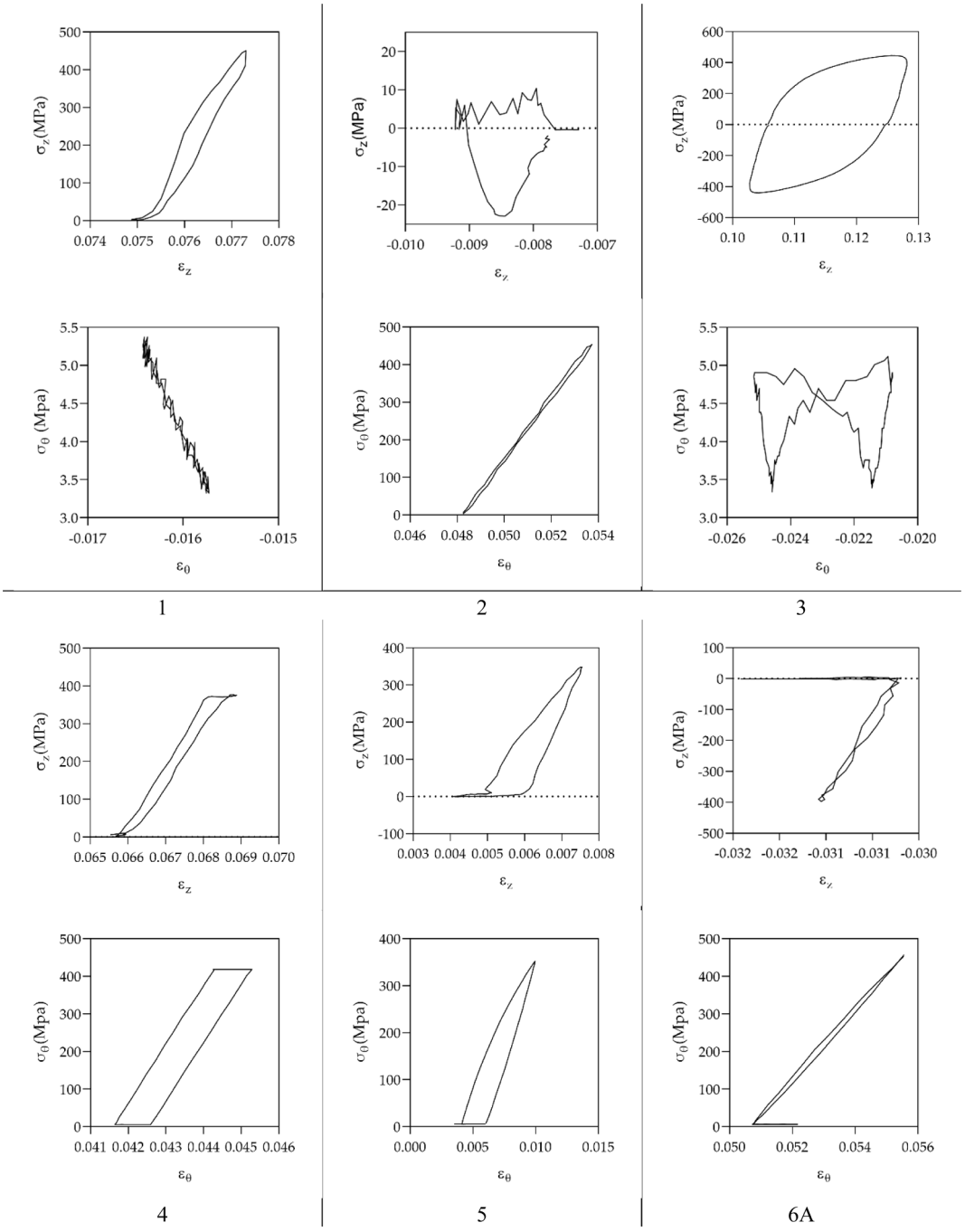

Fig. 3. Loading paths stress–strain curve at half-life fatigue.

maximum. Additionally, it includes the mean stress effect through the maximum value of the normal stress on the critical plane. The model is summarised according to equation (3):

$$\frac{\Delta\gamma_{max}}{2}\left(1+k\frac{\sigma_{n,max}}{\sigma_y}\right)=\frac{\tau'_f}{G}(2N_f)^{b_\gamma}+\gamma'_f(2N_f)^{c_\gamma} \tag{3}$$

where $\Delta\gamma_{max}/2$ is the maximum shear strain amplitude, $\sigma_{n,max}$ is the maximum tensile stress at the critical plane, σ_y is the yield stress, G is the shear modulus, τ'_f is the shear fatigue strength coefficient, b_γ is the shear fatigue strength exponent, γ'_f is the shear fatigue ductility coefficient and c_γ is the shear fatigue ductility exponent and k is a parameter that weighs the normal stress effect on the critical plane.

k parameter is a correction factor which relates the shear strain which appears in a pure torsion test, and the maximum shear strains that appear in a tension–compression test. The values for k parameter are defined as a function of the fatigue life, N_f, according to equation (4) [22].

$$k=\left[\frac{\frac{\tau'_f}{G}(2N_f)^{b_\gamma}+\gamma'_f(2N_f)^{c_\gamma}}{(1+\nu_e)\frac{\sigma'_f}{E}(2N_f)^{b}+(1+\nu_p)\varepsilon'_f(2N_f)^{c}}-1\right]\frac{\sigma'_y}{\sigma'_f(2N_f)^{b}} \tag{4}$$

where υ_e and υ_p are the Poisson ratio in the elastic and plastic regimes respectively, σ'_f is the fatigue strength coefficient, b is the fatigue strength exponent, ε'_f is the fatigue ductility coefficient, c is the fatigue ductility exponent and σ'y is the cyclic yield stress.

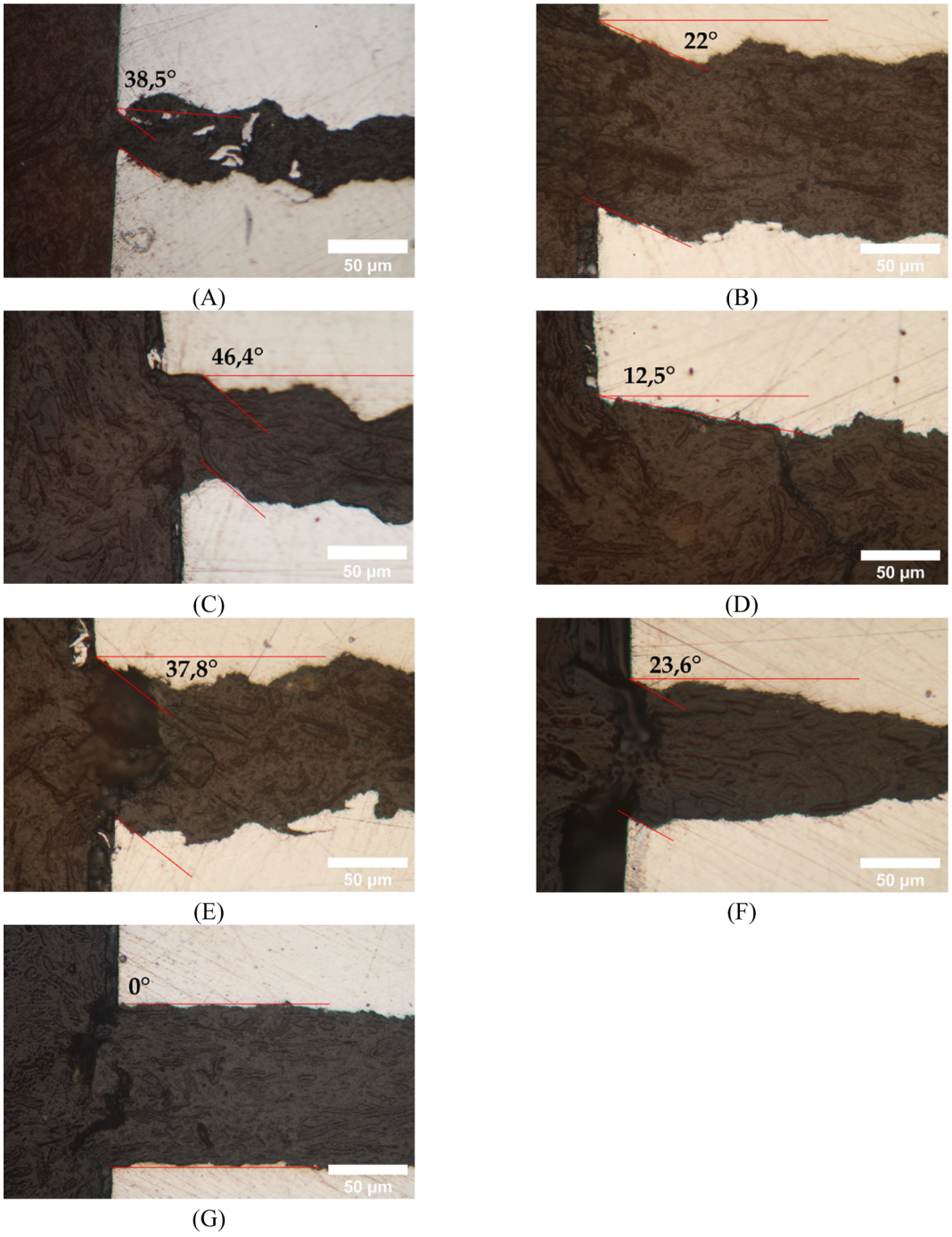

Fig. 4. Crack load path 1(A), 2(B), 3(C), 4(D), 5(E), 6A(F) and 6B(G). Additional details on the different paths are given in Table 4.

3.2. Varvani-Farahani model

Varvani-Farahani (VF) [16] proposed an energy-based parameter equation (5). The parameter includes the damage of the normal and shear component, calculated on the maximum shear strain plane. The critical plane is defined as where the stress and strain Mohr circles are largest during the loading and unloading sections of a cycle. The maximum shear stress and shear strain ranges are obtained on the critical plane, and the maximum normal stress and normal strain ranges correspond at that point of maximum and minimum shear stress and strain along the cycle. The normal and shear components are weighted by the axial and torsional fatigue properties, respectively.

$$DP_{VF} = \frac{1}{\sigma'_f \varepsilon'_f}\Delta\sigma_n\Delta\varepsilon_n + \frac{1}{\tau'_f \gamma'_f}\left(1+\frac{\sigma_{n,m}}{\sigma'_f}\right)\Delta\tau_{max}\frac{\Delta\gamma_{max}}{2} \quad (5)$$

where σ'_f is the fatigue strength coefficient, ε'_f is the fatigue ductility coefficient, τ'_f is the shear fatigue strength coefficient, γ'_f is the shear fatigue ductility coefficient, $\Delta\sigma$ and $\Delta\varepsilon$ are the ranges of the normal stress and strain on the critical plane, respectively; $\Delta\tau$ and $\Delta\gamma$ are the ranges of the shear stress and shear strain respectively; $\sigma_{n,m}$ is the mean value of normal stress on the critical plane.

Gan-Wu-Zhong relates the damage parameter to the fatigue life based on the axial Coffin-Manson equation. Considering the damage parameter as that with the maximum value along the cycle, VF model can be expressed as equation (6) [17].

$$DP_{VF} = f_1 \frac{4\sigma'^2_f}{E}(2N_f)^{2b} + f_2 4\sigma'_f\varepsilon'_f(2N_f)^{b+c} \quad (6)$$

where E is the Young's Modulus, b is the fatigue strength exponent, c is the fatigue ductility exponent, f_1 and f_2 are functions that depend on fatigue properties and are calculated with equation (7).

$$f = \frac{1}{2\dot{\tau}_f\dot{\gamma}_f}\left[\frac{(1+\nu)(1-cos^2(2\theta))}{2}\right] + \frac{1}{2\dot{\sigma}_f\dot{\varepsilon}_f}\left[\frac{1-\nu}{4} + \frac{1}{2}cos(2\theta) + \frac{1+\nu}{4}cos^2(2\theta)\right] \quad (7)$$

where θ is the angle between the specimen axis and the normal plane where the function is evaluated. Function values f_1 and f_2 are obtained as the maximum value of equation (7) considering the Poisson ratio υ with the value in the elastic and plastic regimes regimen respectively, i.e., 0.3 and 0.5 from Table 2. A value of 0.007956 for f_1 and f_2 is obtained for 316 stainless steel.

3.3. Gan-Wu-Zhong model

Gan, Wu and Zhong (LWZ) [17] proposed an energy-based model considering the cyclic plastic strain energy. For in-phase loadings, the damage parameter can be calculated with equation (8).

$$W^c_{p,IP} = 4\sigma^c_a\varepsilon^c_{p,a}\left(\frac{1-n'}{1+n'}\right) + 4\beta\tau^c_a\gamma^c_{p,a}\left(\frac{1-n'_0}{1+n'_0}\right) \quad (8)$$

where σ^c and τ^c are the normal and shear stresses on the critical plane; ε^c_p and γ^c_p are the normal and shear plastic strain on the critical plane; n' and n'_0 are the axial and shear cyclic hardening exponents: $n'=n'_0$ is considered in this work [28]. Materials show a different response to fatigue life depending on the kind of load applied [11,29]. β is a weight coefficient to consider the damage effect under axial and pure torsion loading. This coefficient is defined as the relation between the axial and shear strain fatigue coefficient (ϵ_f/γ_f).

The non-proportional effect on the fatigue life is included with a factor κ* equation (9). This factor κ* considers the loading path effect and the material hardening level.

$$\kappa^* = \sqrt{1 + F_{NP}(1+\alpha_{NP})} \quad (9)$$

where F_{NP} is obtained as the coefficient of the minor and major semi-axe of the minimum ellipse which encloses the loading path and α_{NP} is the NP hardening coefficient. For proportional loadings, the factor value is 1.

To obtain an effective W_{eff} value of the damage parameter which includes the non-proportional effect, multiply the damage parameter equation (8) by the factor κ*.

The damage parameter is related with the fatigue life with equation (10)).

$$\{\Delta W_{eff}\}_{max} = 4(\sigma'_f - \sigma^c_m)\varepsilon'_f\left(\frac{c-b}{c+b}\right)(2N_f)^{b+c} \quad (10)$$

where σ'_f is the fatigue strength coefficient, b is the fatigue strength exponent, ε'_f is the fatigue ductility coefficient, c is the fatigue ductility exponent and σ^c_m is the mean stress applied on the critical plane.

3.4. Liu I and Liu II models

Liu I equation (11) and (12) and Liu II equation (13) and (14) are energy type models [18]. Depending on the failure mode, Liu presents two parameters, one for a normal tension failure, ΔW_I, and another one for shear tension failure, ΔW_{II}. Thus, Liu models can also consider whether the failure is ductile or brittle. Shear stresses and strains will normally show a higher weight for ductile materials and normal stresses and strains will normally show a higher weight for brittle materials [18,30]. For normal tension failure, the plane φ* will be that which maximises the axial work, ΔW_I equation (11). For shear tension failure, the plane φ* will be that which maximises the shear work, ΔW_{II} equation (13). Once φ* is determined, the damage parameter is obtained as the sum of both the axial work and the shear work. The relation between the Liu damage parameters and the fatigue life, N_f, is given by Equations (12) and (14), respectively.

$$\Delta W_I = (\Delta\sigma_n\Delta\varepsilon_n)_{max} + (\Delta\tau\Delta\gamma) \quad (11)$$

where $\Delta\sigma_n$ is the normal stress range, $\Delta\varepsilon_n$ is the normal strain range, $\Delta\tau$ is the shear stress range and $\Delta\gamma$ is the shear strain range.

$$\Delta W_I = 4\sigma'_f\varepsilon'_f(2N_f)^{b+c} + \frac{4\sigma'^2_f}{E}(2N_f)^{2b} \quad (12)$$

where σ'_f is the fatigue strength coefficient, b is the fatigue strength exponent, ε'_f is the fatigue ductility coefficient, c is the fatigue ductility exponent and E is the Young's modulus.

$$\Delta W_{II} = (\Delta\sigma_n\Delta\varepsilon_n) + (\Delta\tau\Delta\gamma)_{max} \quad (13)$$

$$\Delta W_{II} = 4\tau'_f\gamma'_f(2N_f)^{b\gamma+c\gamma} + \frac{4\tau'^2_f}{G}(2N_f)^{2b\gamma} \quad (14)$$

where τ'_f is the shear fatigue strength coefficient, b_γ is the shear fatigue strength exponent γ'_f is the shear fatigue ductility coefficient, c_γ is the shear fatigue ductility exponent and G is the shear modulus.

3.5. Prediction error

The model fatigue life prediction capacity is evaluated by studying the mean and standard deviation of the error. The error is defined as the difference between the predicted and experimental fatigue life in a logarithmic scale equation (15).

$$\text{error} = \log_{10}(N_{mod}) - \log_{10}(N_{exp}) \quad (15)$$

where N_{mod} is the fatigue life predicted by the model and N_{exp} is the experimental fatigue life.

The crack plane angle error is defined as the angle difference between the normal vector and the plane of the predicted and experimental crack plane, divided by 90°.

4. Results and discussion

The fatigue life estimates for each of the models studied are shown in Fig. 5. FS results are shown with blue squares, VF results with green triangles, LWZ results with black circles, Liu I results with yellow blades and Liu II results with purple crosses. A title to identify the test is included next to each dataset.

Most of the fatigue life estimates are fitted within scatter bands of two. As previously mentioned, the stresses on the outer surface are lower than on the inner surface for the loading path which includes an inner pressure. This way, from the set of tests, loading paths 1 and 3 show a better model prediction, with most of the fatigue life calculated on the conservative side. LWZ shows the most conservative values, except for test 1, with higher fatigue life. This is probably because of the lower plastic strain which appears at that regime. Although the mean strain produced by the loading path is high, as observed in Table 4, the effect on the fatigue life prediction is low, considering that the strain amplitude increment at middle fatigue life is similar to the one after the first number of cycles after stabilisation. This seems to agree with other studies on stainless steels [31]. Liu models do not include any additional terms to include the effects of mean stress or strain. Liu's model good predictions suggest that mean stress has a low influence on fatigue predictions in 316 stainless steel at these fatigue life intervals, as observed by Zhang et al. [32] in 316L. As previously mentioned, the damage parameter is defined as the maximum in all planes, so

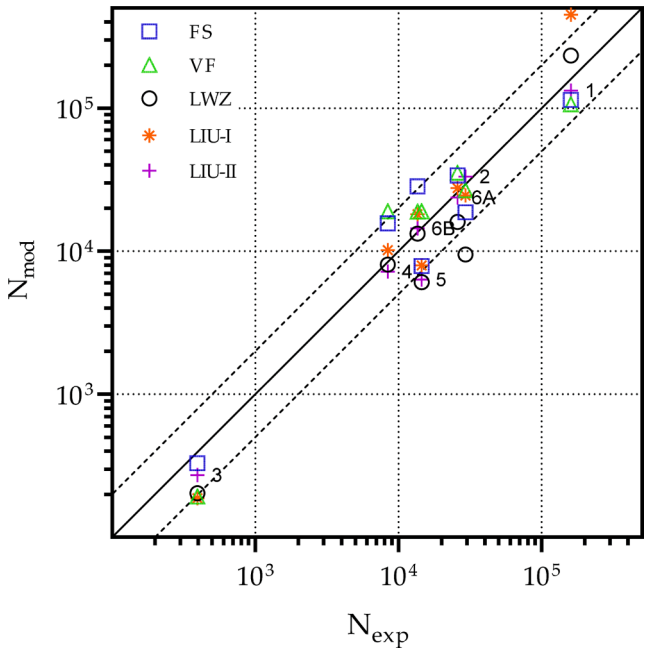

Fig. 5. Critical plane model fatigue life prediction for uniaxial and biaxial loading paths tests in 316 stainless steel.

differences between Liu I and II come from the cyclic fatigue properties considered, uniaxial for Liu I and torsional for Liu II. The superior fit of Liu II estimates suggests that this material is better characterised by using shear values for both strain and stress. Tests 2 and 6A, both with the same inner pressure, return approximately the same fatigue life, although test 6 includes a compressive step on the cycle. This seems to indicate that a compressive part of the cycle has a lower effect on the fatigue life. Comparing the fatigue life values between loading paths 5 and 6, it appears that tensile load increases the strain range in both direction z and θ, while a compressive load reduces it. As described above, inner pressure induced cracks to nucleate along the longitudinal direction (Z direction in Fig. 1). A compressive load along the Z direction would induce some degree of buckling thereby contributing to the opening of such cracks. This can be observed by comparing the fatigue life of paths 2 and 6A. However, the reduction in fatigue life from path 2 to path 6A is surprisingly small (only 12%). This suggests that for the loads tested, the combined effect of compressive load together with inner pressure in alternative steps (paths 6A and 6B) is lower than expected. Indeed, a ~10% increment in the applied load (path 6A to path 6B) induces a much drastic reduction in fatigue life (47% reduction) than applying inner pressure and compression instead of only inner pressure.

The probability density function (PDF) of the fatigue life error was computed. The PDF results are shown in Fig. 6, curves closer to zero mean error; and with lower deviation, indicate better accuracy of the model. The negative error values indicate conservative predictions, and non-conservative with positive values. FS, VF and Liu I return similar results with predictions inside the scatter bands (Fig. 6), but with higher deviation. LWZ gives the most conservative results with lower scatter, and Liu II generates less conservative values than LWZ but with the lowest scatter among the studied models. These results are in agreement with previous studies performed on 316 stainless steel with axial torsional loadings, where Liu obtained a better correlation with ΔW_{II} than ΔW_{I} [33]. These results are complementary to those presented

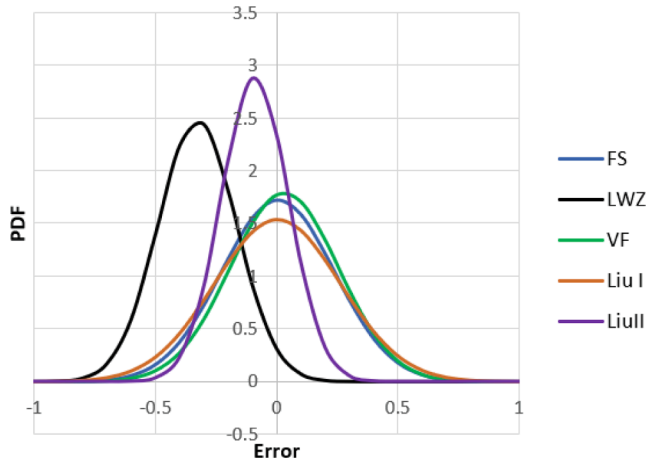

Fig. 6. Probability density function of prediction error for 316 stainless steel.

previously [17] where the proposed model was not checked against FS model, which, in terms of citations since it was presented, is probably the most accepted model.

Table 5 compares the experimental initial crack growth plane (blue) with that defined by the critical plane models studied (red) for each of the tests. For the cases of loads applied in one direction only, the predictions are better than in the cases of load paths with loads applied in two directions.

A plane deviation error is defined based on the angle formed between the experimental and predicted plane normal vectors. The difference between the angles is divided by 90°, thus considering a 100% error as one where the predicted plane is completely perpendicular to the experimental plane.

Combining each model's deviation errors, the total sum for the different models is as follows: FS 233.75%, VF 277.38%, LWZ 264.84%, Liu I and II 236.33%. Considering these values, the best crack angle predictions have been obtained with the FS model but Liu I and Liu II were extremely close. The good predictions of FS and Liu models are probably connected to the failure mode being predominantly ductile for the multiaxial conditions explored. The very similar sum of deviations errors for those models reinforces the idea of ductile failure mechanisms prevailing on the 316 steel. The worst predictions were obtained for biaxial tests, where in all cases, crack growth was perpendicular to the θR plane. Evaluating the cracking angle is important from an engineering design point of view because it contributes to the complete solution of the crack growth problem and assists in the selection of the most appropriate non-destructive tests [34].

As observed with the above results, from the different model tested, there is no single critical plane model that can produce best predictions in terms of fatigue life and cracking orientation. There exists alternative critical plane models able of predicting accurately both the life and the orientation. They follow a more empirical route, where a large amount of similar tests are required to perform predictions (see e.g. [2,35]. This is useful for a limited number of industries that have large databases of material behaviour under similar types of multiaxial conditions to those conditions investigated. Nevertheless the philosophy of that approach differs from most standard routes (critical plane criteria based on stresses, based on strains and based on strain energy density) that are founded on the physical observations that cracks initiate and grow on preferred planes [22]. These more standard models require some material properties gathered from simple uniaxial tests. Unfortunately, no single model based on the failure mechanism has been yet proposed that

Table 5
Models critical plane prediction (red) vs experimental crack angle (blue).

	FS	VF	LWZ	LIU I-II
1	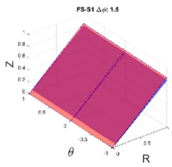	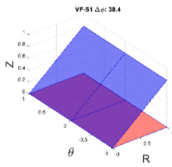	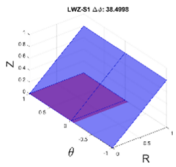	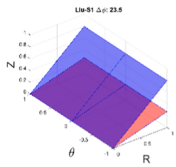
2	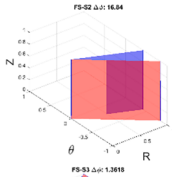	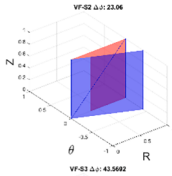	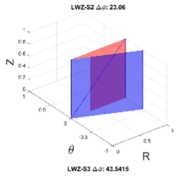	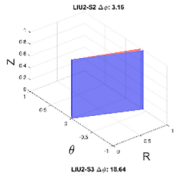
3	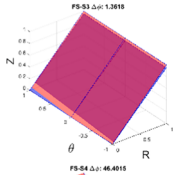	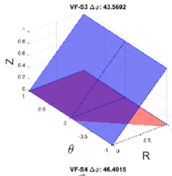	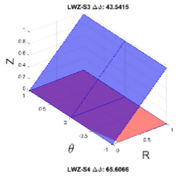	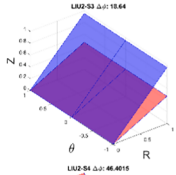
4	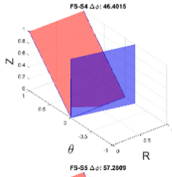	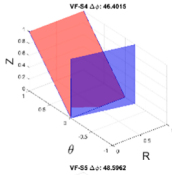	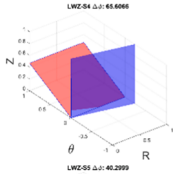	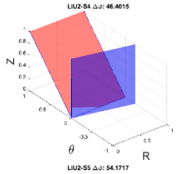
5	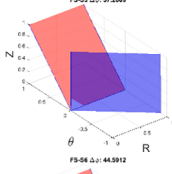	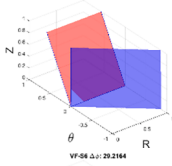	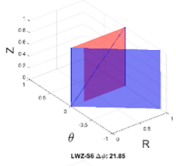	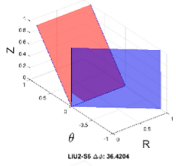
6A	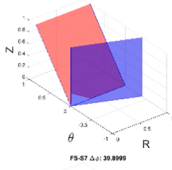	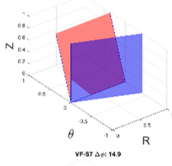	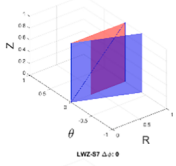	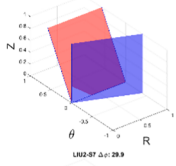
6B	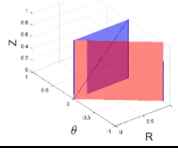	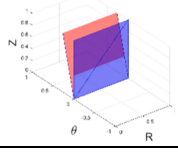	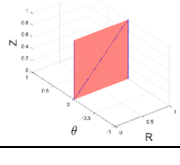	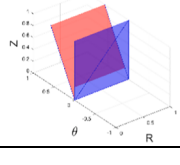

can accurately predict the fatigue life and the cracking orientation for a wide range of materials subjected to a wide range of multiaxial configurations [20,25].

5. Conclusions

In this work, the multiaxial fatigue behaviour of 316 stainless steel has been analysed. Tests performed include high mean deformation values and non-proportional load paths. Critical plane methods have been applied to study the fatigue life of the material. Models defined by Fatemi-Socie, Gan-Wu-Zhong, Varvani-Farahani, Liu I and Liu II have been presented. In addition to evaluating fatigue life, the critical planes were also used to predict crack growth angles for different multiaxial paths. This is an essential feature of critical plane models that is often ignored but that is key from a design against fatigue point of view. Results indicate low sensitivity of the compressive part of the cycle for the L-shape loading path. Compression tends to reduce the strain range of the cycle, thus generating a higher fatigue life. Conversely, the tension part of the L-shape loading path increases the strain range. The combined effect of compression with inner pressure in alternative steps was found surprisingly low. The best fatigue life estimates have been obtained with the Liu II model, agreeing with previous results performed on this material. On the other hand, the best initial crack growth angle estimates were obtained using the Fatemi-Socie model. A newly proposed critical plane model, named Gan-Wu-Zhong, is studied and applied in this work, showing good correlation with the results, but with poor prediction in the high cycle fatigue regime.

Declaration of Competing Interest

The authors declare that they have no known competing financial interests or personal relationships that could have appeared to influence the work reported in this paper.

Acknowledgements

Financial support of Programa Operativo FEDER from the Junta de Andalucia (Spain) through grant reference UMA18-FEDERJA-250 is greatly acknowledged. Support from the Oceanic Engineering Research Institute from Malaga is also acknowledged. Industrial support from

Bettergy and Dr Nicolas Ordoñez is greatly acknowledged, as well as access to different structures and materials in the energy industry. We would also like to acknowledge funding for open access charge: Universidad de Malaga / CBUA.

References

[1] J. Papuga, M. Vargas, M. Hronek, Evaluation of uniaxial fatigue criteria applied to multiaxially loaded unnotched samples, Eng. Mech. 19 (2012) 99–111.

[2] A. Cruces, P. Lopez-Crespo, B. Moreno, F. Antunes, V Multiaxial Fatigue Life Prediction on S355 Structural and Offshore Steel Using the SKS Critical Plane Model, Metals (Basel) 8 (12) (2018) 1060, https://doi.org/10.3390/met8121060.

[3] A.S. Cruces, M. Mokhtarishirazabad, B. Moreno, M. Zanganeh, P. Lopez-Crespo, Study of the biaxial fatigue behaviour and overloads on S355 low carbon steel, Int. J. Fatigue 134 (2020) 105466, https://doi.org/10.1016/j.ijfatigue.2019.105466.

[4] X. Chen, Q. Gao, X.F. Sun, Damage analysis of low-cycle fatigue under non-proportional loading, Int. J. Fatigue 16 (1994) 221–225.

[5] P. Lopez-Crespo, S. Pommier, Numerical analysis of crack tip plasticity and history effects under mixed mode conditions, J. Solid Mech. Mater. Eng. 2 (2008) 1567–1576.

[6] S. Kida, T. Itoh, M. Sakane, M. Ohnami, D.F. Socie, Dislocation structure and non-proportional hardening of type 304 stainless steel, Fatigue Fract. Eng. Mater. Struct. 20 (1997) 1375–1386.

[7] M. Firat, R. Kozan, M. Ozsoy, O.H. Mete, Numerical modeling and simulation of wheel radial fatigue tests, Eng. Fail. Anal. 16 (2009) 1533–1541.

[8] M. Firat, U. Kocabicak, Analytical durability modeling and evaluation-complementary techniques for physical testing of automotive components, Eng. Fail. Anal. 11 (2004) 655–674.

[9] A. Carpinteri, A. Spagnoli, S. Vantadori, Multiaxial fatigue life estimation in welded joints using the critical plane approach, Int. J. Fatigue 31 (2009) 188–196.

[10] R. Branco, J.D. Costa, J.A.M. Ferreira, C. Capela, F.V. Antunes, W. Macek, Multiaxial fatigue behaviour of maraging steel produced by selective laser melting, Mater. Des. 201 (2021), 109469.

[11] D. Socie, Multiaxial Fatigue. *Multiaxial Fatigue* (1999) 113.

[12] T. Morishita, T. Itoh, Z. Bao, Multiaxial fatigue strength of type 316 stainless steel under push-pull, Reversed torsion, Cyclic inner and outer pressure loading, Int. J. Press. Vessel. Pip. 139–140 (2016) 228–236.

[13] S. Holmström, R. Pohja, A. Nurmela, P. Moilanen, P. Auerkari, Creep and creep-fatigue behaviour of 316 stainless steel, Procedia Eng. 55 (2013) 160–164.

[14] D. Jin, D.J. Tian, J.H. Li, M. Sakane, Low-cycle fatigue of 316L stainless steel under proportional and nonproportional loadings, Fatigue Fract. Eng. Mater. Struct. 39 (2016) 850–858.

[15] A. Fatemi, D.F. Socie, A Critical Plane Approach to Multiaxial Fatigue Damage Including out-of-Phase Loading, Fatigue Fract. Eng. Mater. Struct. 11 (1988) 149–165.

[16] A. Varvani-Farahani, New energy-critical plane parameter for fatigue life assessment of various metallic materials subjected to in-phase and out-of-phase multiaxial fatigue loading conditions, Int. J. Fatigue 22 (2000) 295–305.

[17] L. Gan, H. Wu, Z. Zhong, Use of an energy-based/critical plane model to assess fatigue life under low-cycle multiaxial cycles, Fatigue Fract. Eng. Mater. Struct. 42 (2019) 2694–2708.

[18] K.C. Liu, J.A. Wang, An energy method for predicting fatigue life, crack orientation, and crack growth under multiaxial loading conditions, Int. J. Fatigue 23 (2001) 129–134.

[19] A. Carpinteri, L. Pook, Fatigue crack paths, Fatigue Fract. Eng. Mater. Struct. 28 (2005).

[20] A. Carpinteri, F. Berto, Y. Hong, T. Palin-Luc, Foreword: Fatigue Crack Paths 2018 (after CP 2018), Int. J. Fatigue 128 (2019) 105239, https://doi.org/10.1016/j.ijfatigue.2019.105239.

[21] ASTM E2207-08 08 (2014) 2–9.

[22] D.F. Socie, G.B. Marquis, Multiaxial fatigue, 1st ed., Society of Automotive Engineers Inc, Warrendale, PA (USA), 2000.

[23] A. Ayob, M.K. Elbasheer, Optimum autofrettage pressure in thick cylinders, J. Mek. (2007) 1–14.

[24] S. Timoshenko, J. Goodier, Theory of elasticity, Third.; Mcgraw-Hill, New York, 1980.

[25] A. Karolczuk, E. Macha, A review of critical plane orientations in multiaxial fatigue failure criteria of metallic materials, Int. J. Fract. 134 (2005) 267–304.

[26] P. Lopez-Crespo, B. Moreno, A. Lopez-Moreno, J. Zapatero, Study of crack orientation and fatigue life prediction in biaxial fatigue with critical plane models, Eng. Fract. Mech. 136 (2015) 115–130.

[27] T. Wehner, A. Fatemi, Effects of mean stress on fatigue behaviour of a hardened carbon steel. Int. J. Fatigue 3 (1991) 241–248.

[28] J. Li, Z.P. Zhang, Q. Sun, C.W. Li, R.S. Li, A simple relationship between axial and torsional cyclic parameters, J. Mater. Eng. Perform. 20 (2011) 1289–1293.

[29] N. Shamsaei, M. Gladskyi, K. Panasovskyi, S. Shukaev, A. Fatemi, Multiaxial fatigue of titanium including step loading and load path alteration and sequence effects, Int. J. Fatigue 32 (2010) 1862–1874.

[30] L. Reis, B. Li, M. de Freitas, Crack initiation and growth path under multiaxial fatigue loading in structural steels, Int. J. Fatigue 31 (11-12) (2009) 1660–1668.

[31] X. Chen, K. An, K.S. Kim, Low-cycle fatigue of 1Cr-18Ni-9Ti stainless steel and related weld metal under axial, torsional and 90 out-of-phase loading, Fatigue Fract. Eng. Mater. Struct. 27 (2004) 439–448.

[32] W. Zhang, R. Akid, Mechanisms and fatigue performance of two steels in cyclic torsion with axial static tension/compression, Fatigue Fract. Eng. Mater. Struct. 20 (1997) 547–557.

[33] K. Liu, A method based on virtual strain energy parameters for multiaxial fatigue life prediction. ASTM, 1993, STP 1191, pp. 67–84.

[34] A. Carpinteri, R. Brighenti, A. Fatemi, L. Susmel, Crack Paths 2015 (after CP 2015), Eng. Fract. Mech. 167 (2016) 1.

[35] S. Suman, A. Kallmeyer, J. Smith, Development of a multiaxial fatigue damage parameter and life prediction methodology for non-proportional loading, Frat. ed Integrità Strutt. 38 (2016) 224–230.